International Journal of Disaster Risk Reduction xxx (xxxx) xxx–xxx

Contents lists available at ScienceDirect

International Journal of Disaster Risk Reduction

journal homepage: www.elsevier.com/locate/ijdrr

# An integrated method to extract collapsed buildings from satellite imagery, hazard distribution and fragility curves

Luis Moya[a,*], Erick Mas[a], Bruno Adriano[a], Shunichi Koshimura[a], Fumio Yamazaki[b], Wen Liu[b]

[a] International Research Institute of Disaster Science, Tohoku University, Aoba 468-1-E301, Aramaki, Aoba-ku, Sendai 980-0845, Japan
[b] Department of Urban Environment System, Chiba University, Chiba 263-8522, Japan

ARTICLE INFO

*Keywords:*
The 2011 Great East Japan Tsunami
SAR images
Collapsed buildings

ABSTRACT

Remote sensing satellite imagery plays an important role in estimating collapsed buildings in the aftermath of a large-scale disaster. However, some previous methodologies are restricted to using specific radar sensors. Others methods, such as machine learning algorithms, require training data, which are extremely difficult to obtain immediately after a disaster. This paper proposes a novel method to extract collapsed buildings based on the integration of satellite imagery, the spatial distribution of a demand parameter, fragility functions, and a geospatial building inventory. The proposed method is applicable regardless of the type of radar sensor and does not require any training data. The method was applied to extract buildings that collapsed during the 2011 Great East Japan Tsunami. The results showed that the proposed method is effective and consistent with the surveyed building damage data.

## 1. Introduction

The extraction of infrastructure damage in the aftermath of a large-scale disaster is critical for quick response measures such as relief distribution. Thus, the most accurate the estimation is, the better the decisions will be during an emergency. Remote sensing technology, such as optical and synthetic aperture radar (SAR) satellites, has been used during several disasters to retrieve the extent of the damage. Basic approaches rely on identifying changes between two images taken before and after a disaster event. These approaches are based on the assumption that the changes are correlated with the effects of the earthquake. The averaged pixel difference, correlation coefficient, and coherence between a pair of images are parameters that are often used to detect changes [1–4]. Here, the main challenge is to set a threshold that properly separates the damaged and non-damaged areas.

According to the Union of Concerned Scientists [5], of 1459 satellites currently in orbit, there were 396 earth observation satellites on December 31, 2016. This number of satellites indicates that the near real-time monitoring of affected areas in the aftermath of a natural disaster is becoming a reality. In fact, satellite imagery is currently available within few days. For instance, the Open Data Program of Digital Globe provides optical imagery of affected areas to support disaster response [6]. Therefore, it is necessary to implement an effective methodology to detect damaged areas.

Several methods have been proposed in previous studies for the extraction of damaged areas. A significant number of these methods rely on change detection between a pair of satellite images. Liu et al. [1] introduced a $z$ factor to evaluate the changes between a pair of TerraSAR-X intensity images. This factor is a linear combination of the absolute value of the normalized difference of backscattering and the correlation coefficient. Both parameters were calculated using a moving window. Here, the changes were evaluated at the pixel- and building-unit-levels using a threshold for the $z$ factor. Gokon et al. [7] proposed a damage function $F_{R_m}$ in terms of a mean value of a correlation coefficient within an object $R_m$. Both methods, the $z$ factor and $F_{R_m}$, showed good agreement with the actual damage situation. However, it was later pointed out that the methodologies need calibration when other types of satellite sensor are used [8,3]. To overcome the limitations of using a manual threshold, training samples have been used for calibration. Wieland et al. [9] evaluated the Support Vector Machine (SVM) method to detect the changes produced by earthquakes and tsunamis. In this work, this method was identified as superior in terms of the multi-dimensional change feature space and the definition of a decision boundary. Nevertheless, the main problem of using supervised classification techniques in damage detection is the need of training samples. The most reliable sources of training data are field surveys; however, in the aftermath of a disaster, the main effort is focused on relief distribution and first aid. In most cases, information regarding the damage state to infrastructure is available after several weeks. Training data from the visual inspection of optical images is sometimes used in the

* Corresponding author.
*E-mail address:* lmoyah@irides.tohoku.ac.jp (L. Moya).

https://doi.org/10.1016/j.ijdrr.2018.03.034
Received 26 October 2017; Received in revised form 5 March 2018; Accepted 30 March 2018

absence of survey data; however, these data introduce biases because collapsed buildings without significant damage to the roof are difficult to detect.

Other technologies are used to retrieve information related to the intensity of the disaster. For instance, GNSS and strong motion networks are used to record the permanent ground deformation and transient waves due to large earthquakes [10–12]. Areas inundated by tsunamis can be estimated from numerical simulation [13] in near real-time for early warning system purposes [14,15]. From now on, the term engineering demand parameter (EDP) will refer to the intensity of the natural hazard. Thus, EDP can represent the peak ground acceleration for an earthquake event or the inundation depth for a tsunami event. If the spatial distribution of EDP is available, it is possible to infer which areas are more likely to experience damage to their infrastructure. A product of risk analysis is a damage map of the affected areas in terms of probabilities, where the spatial distribution of EDP is one input [16–20]. Here, based on surveys of previous events and/or numerical simulations, a relationship between the probability that an asset will experience a certain level of damage and a certain level of the EDP is often used. Such a relationship is often called a fragility curve. Thus, a fragility curve gives the probability that an asset will reach or exceed certain level of damage under a given level of EDP [21–24,13]. The limitation of the use of fragility curves and the distribution of EDP for damage detection is that this approach provides aggregate values in terms of probabilities, that is, a percentage of building damage. Therefore, it is not possible to obtain a damage map at the resolution of a building unit.

In this study, a novel damage classification method is proposed. Here, an integrated geospatial database that includes satellite imagery, the spatial distribution of EDP, fragility curves, and a building inventory is used to perform damage classification without the need for training data. The next section describes the details of the methodology. Then, the extraction of the collapsed buildings due to the 2011 Great East Japan Tsunami are presented as a case study.

## 2. Principle of the method

The following method is an hybrid approach for mapping collapsed buildings that combines fragility curves and change detection. The method consists of finding the best function threshold of certain features extracted from satellite images with the aim of detecting changes. The main constraint in the definition of the threshold function is that the spatial distribution of detected changes should be consistent with the spatial distribution of EDP. That is, a greater ratio of change should be detected in areas with large EDP; similarly, a low ratio of change should be observed in areas with low EDP. To control the ratio of change, a fragility function is used as reference. A number of fragility functions for diverse hazards have been proposed in previous studies. The key principle of the proposed method is illustrated in Fig. 1, and the steps are as follows.

1. Input the satellite imagery and the building inventory. Here, the satellite imagery is inserted into the system for further analysis. For the purpose of change detection, pre-event and a post-event satellite images should be inserted. Recall that the images must be ready for use. That is, it is implied that pre-processing has been performed. For instance, synthetic aperture radar (SAR) images require calibration, speckle filtering and terrain correction. Furthermore, the geographical location of the buildings is also required.
2. Feature extraction. In this step, a first database is prepared. The features used for detecting changes in the satellite imagery at the location of the buildings are calculated. For SAR images, common features used to detect changes are the differences in pixel values, correlation coefficients, and the coherence between the pre- and post-event imagery. The constructed database consists of a matrix in which each row represents a building measurement. The first column contains the building code, and the remaining columns contain the extracted features.
3. Function threshold candidate. The main purpose of this method is to define a threshold function $T$ that will be used as a decision boundary to infer whether a building exhibits changes. Fig. 1 shows a two-dimensional database example where the threshold function is a line. The optimal threshold function is defined within an iterative process under the constraint explained in the following steps. Using the function threshold, each building will be classified as either *changed* or *non-changed*.
4. Inventory of change detected and EDP. In this step a second database is prepared in which two sets of information are stored for each building: (1) the change classification based on a candidate threshold function and (2) the *edp*. *edp* denotes a particular realization of EDP. Note that at this step, the spatial distribution of EDP is inserted to the system.
5. Calculation of the cost function. From the second database, the classified buildings are grouped into bins by ranges of EDP. For each bin, the ratio of buildings classified as *changed* ($cr$) and the bin-average EDP are calculated. Then, the level of matching between the $cr$ values and the fragility function $F$ are measured by calculating the cost function $C$:

$$C = \sum_{i}^{N_b} (cr_i - F_i)^2 \tag{1}$$

where $N_b$ denotes the number of bins. $cr_i$ denotes the ratio of buildings classified as *changed* for bin $i$. $F_i$ denotes the failure probability for the $i$-th bin-averaged EDP calculated from the fragility function.

The optimal threshold function is that which yields the minimum value of $C$, which can be found from an iterative optimization process. Thus, steps 3–5 are continuously repeated within a loop until the optimal threshold function is found. Note that although the extraction of *edp* for each building is shown in step 4, this task is performed once because it is independent of the threshold function.

## 3. Experimental result and analysis

### 3.1. Case study and dataset

To demonstrate the performance of the method, the 2011 Great East Japan Tsunami event was selected as a case study. A Mw 9.0 earthquake occurred on March 11, 2011 off the Pacific Coast of Japan. This event was an interplate earthquake associated with the subduction of the Pacific plate beneath the North American plate at the Japan Trench. The event produced an extensive coseismic slip that generated a huge tsunami. The east coast was severely affected with more than 400,000 damaged buildings.

Fig. 2 shows a pair of TerraSAR-X images of the coastal zone of Tohoku, Japan. The images were taken on October 21, 2010 (pre-event) and March 13, 2011 (post-event). Both images were captured with HH polarization in a descending path and with the same incident angle (37.3) at the center. The images were acquired in StripMap mode. After an orthorectification, the images were resampled to a resolution of 1.25 m. Then, the images were transformed to a sigma naught ($\sigma^0$) value, and an enhanced Lee filter with window size $3 \times 3$ was applied. Further information about the TerraSAR-X images can be found in [1].

Fig. 3 depicts the spatial distribution of the inundation depth and a survey of building damage levels within the affected area. Both of these informations were provided by the Ministry of Land, Infrastructure and Transportation (MLIT). The inundation depth information had a resolution of 100 m, and the maximum inundation depth within the study areas was 21.8 m. In this case study, the inundation depth represents the EDP. The damage states of the affected buildings were classified

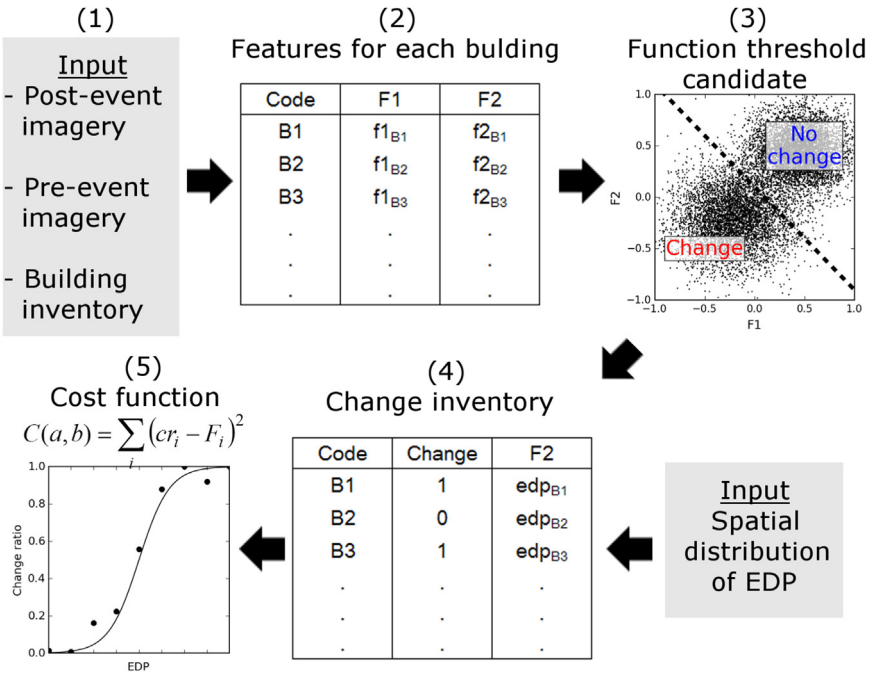


**Fig. 1.** Schematic illustration of the flowchart of the proposed method.

into 7 categories, the descriptions of which are shown in Table 1. The surveyed building damage inventory is used as a ground truth data to compare the results of the proposed method. Due to resolution limitations, SAR imagery cannot detect minor damage such as cracks or even the failure of certain structural elements. Thus, the damage states was merged to represent collapsed and non-collapsed buildings.

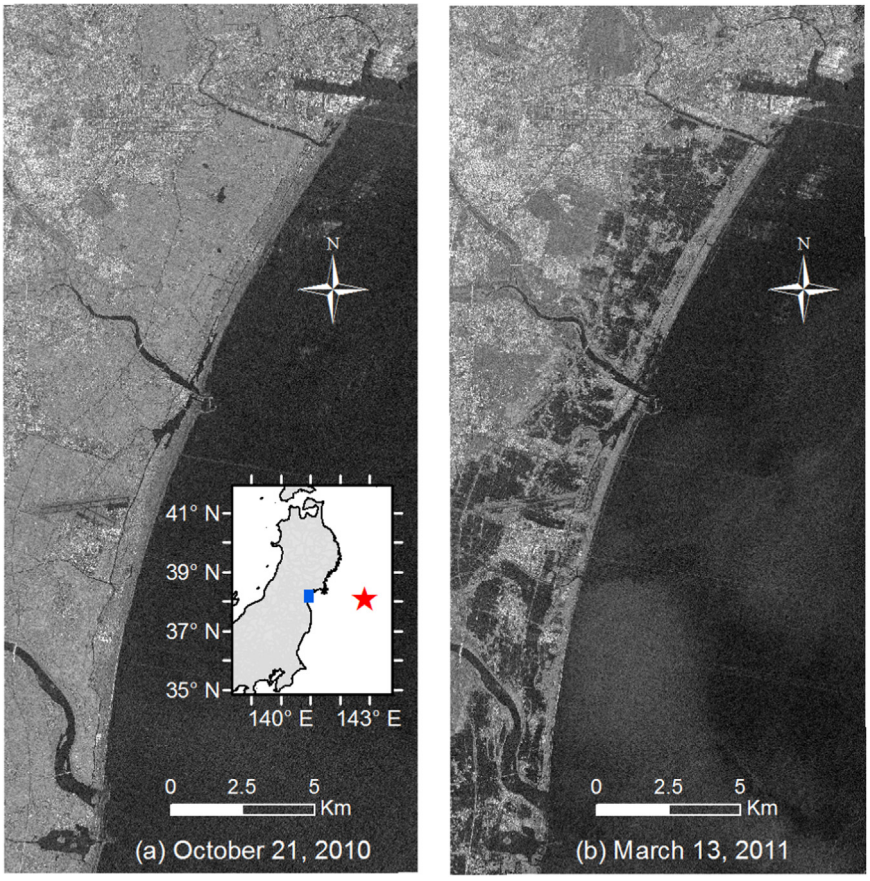


**Fig. 2.** (a) Pre-event TSX image taken on October 21, 2010. The inset shows the location of the study area (rectangle mark) and the epicenter of the earthquake (star mark); (b) Post-event TSX image taken on March 13, 2011.

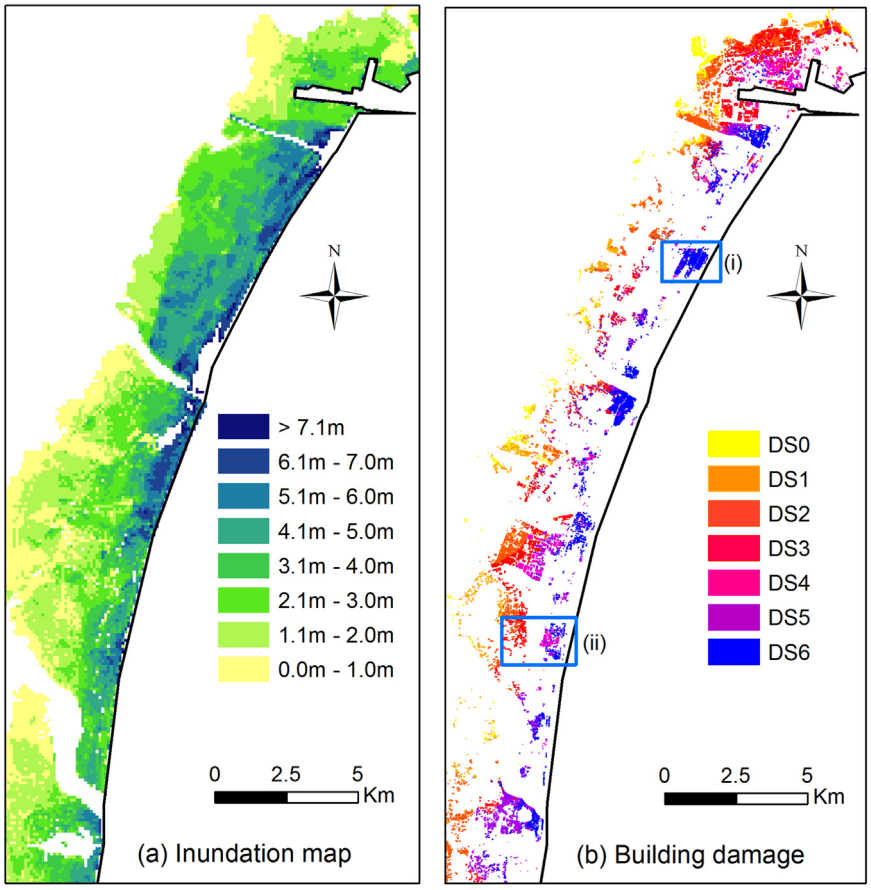


**Fig. 3.** (a) Inundation map caused by the tsunami; (b) Spatial distribution of the buildings damage surveyed by the MLIT (DS: damage state).

**Table 1**
Damage state levels and their description.

| Damage level | Classification |
|---|---|
| 0 | No presence of damage |
| 1 | Minor damage |
| 2 | Moderate damage |
| 3 | Major damage |
| 4 | Complete damage |
| 5 | Collapsed |
| 6 | Washed away |

### 3.2. Fragility functions

The fragility function used in the methodology must be consistent with the concerned disaster event. Thus, in this study, two fragility functions constructed for tsunami events are tested. The first fragility function was proposed by Koshimura et al. [13]. The fragility function was constructed from the numerical modeling of tsunami inundation and a surveyed building damage inventory obtained from Banda Aceh, Indonesia. In this study, a normal cumulative distribution function ($\Phi$) was proposed:

$$F(edp) = \Phi\left(\frac{edp - 2.99}{1.12}\right) \quad (2)$$

The second fragility function tested in this study was proposed by Suppasri et al. [23]. In this study, a surveyed building damage inventory from the 2011 Great East Japan Tsunami event was used. A rich building damage inventory from the all tsunami affected areas was available. Several sets of fragility functions were constructed according to building material. Each set consists of 6 fragility functions for the 7 damage levels shown in Table 1. Here, we used the fragility function for damage level 6 from the set constructed from the all buildings (i.e., no distinction of the building material). Unlike Koshimura et al. [13], a lognormal cumulative distribution function was proposed in this study:

$$F(edp) = \Phi\left(\frac{\ln edp - 1.2244}{0.5723}\right) \quad (3)$$

In order to evaluate the effect of the fragility function in the results, a linear function and a logistic function were tested as fragility functions as well:

$$F(edp) = \frac{edp}{edp_m} \quad (4)$$

$$F(edp) = \frac{1}{1 + e^{-k(edp - 0.5edp_m)}} \quad (5)$$

where $edp_m$ is the lowest $edp$ that produces a 100% probability of damage for the linear function. For the logistic function, $edp_m$ is twice the $edp$ that produces a 50% probability of damage, and $k$ is the steepness of the curve.

### 3.3. Detection of collapsed buildings

Two features were extracted from the pair of SAR images: the difference in backscattering $d$ and the correlation coefficient $r$. Both features were constructed for each building. The features were constructed using the backscattering coefficient located within a rectangular box, which was constructed as follows: First, a polygon $P$ that encloses the building footprint within a specified distance is created. In this study, a distance of 5 m was used. This process is commonly called buffering in geospatial analysis. Then, the rectangular box is defined as the smallest bounding rectangle that contains the polygon $P$. The reason for using an

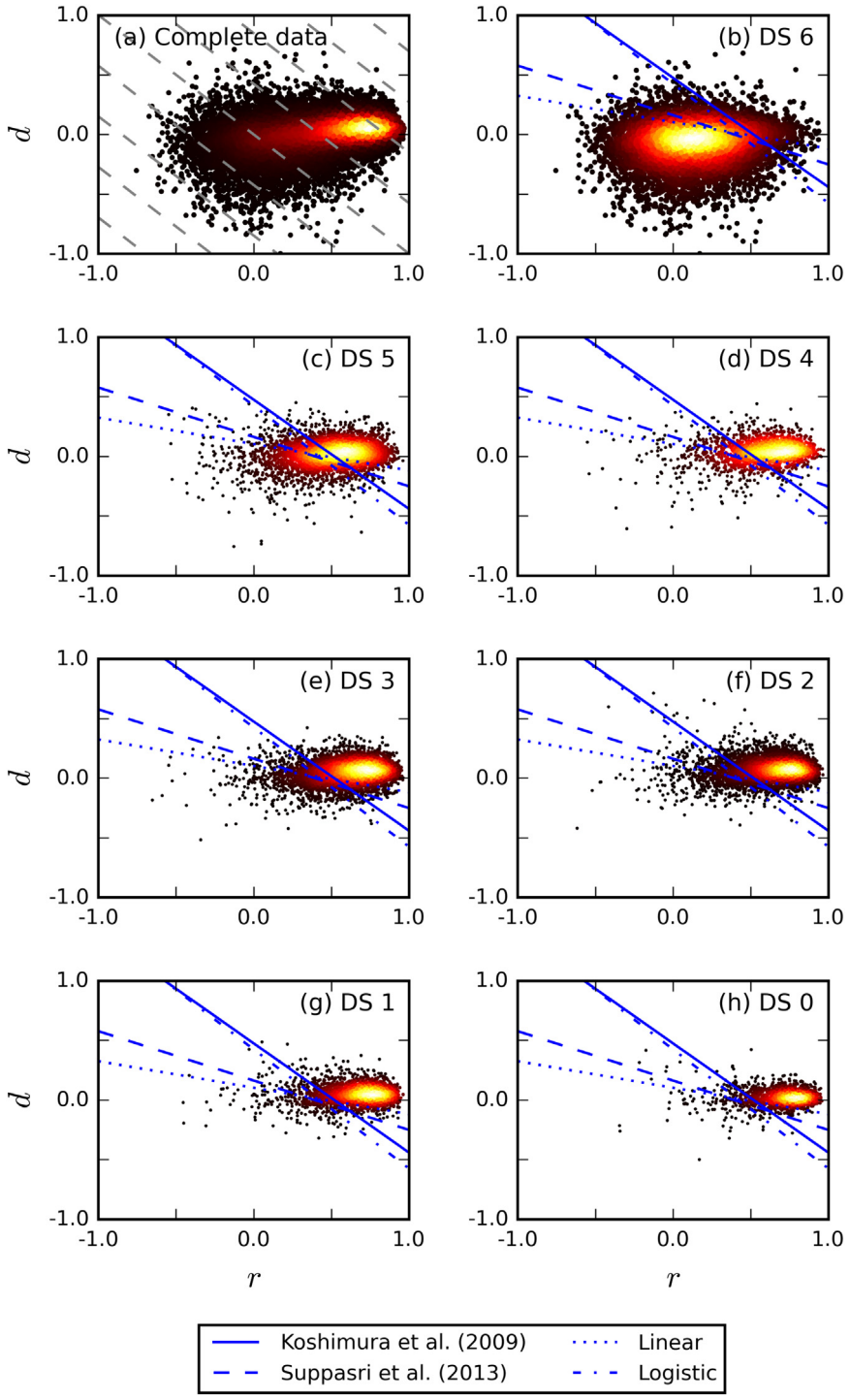


**Fig. 4.** Scatter plot of correlation coefficient ($r$) vs normalized difference of backscattering ($d$). (a) The complete dataset; (b)–(h) Separated by different damage state (DS) according to MLIT. The solid, dotted, dashed and dash-dotted lines in (b)–(h) depict the calibrated linear thresholds resulting from the methodology.

extended building footprint is the nature of SAR images. SAR systems have a side-looking imaging geometry, and thus, this feature causes effects outside the building footprint such as *shadows* for areas hidden from the radar illumination and *layover* due to double bouncing and scattering of building walls and roofs. It has been indicated that shadowing and layover are affected if the building is damaged [25]. The features $d$ and $r$ are calculated as follows:

$$d_i = \frac{1}{max(|\boldsymbol{d}|)} \frac{1}{N_i} \sum_{j}^{N_i} (Ia_j - Ib_j) \tag{6}$$

$$r_i = \frac{N_i \sum_{j=1}^{N_i} Ia_j Ib_j - \sum_{j=1}^{N_i} Ia_j \sum_{j=1}^{N_i} Ib_j}{\sqrt{N_i \sum_{i=1}^{N_i} Ia_j^2 - \left(\sum_{i=1}^{N_i} Ia_j\right)^2} \sqrt{N_i \sum_{i=1}^{N_i} Ib_j^2 - \left(\sum_{i=1}^{N_i} Ib_j\right)^2}} \tag{7}$$

where the index $i$ refers to the $i$-th building; the index $j$ refers to the $j$-th pixel within the rectangular box of building $i$; $Ia$ and $Ib$ are the backscattering coefficient of the post- and the pre-event SAR images, respectively; and $N_i$ denotes the number of pixels within the rectangular box of building $i$. $\boldsymbol{d}$ is a vector that contains the $d_i$ of all buildings. Note that the term $max(|\boldsymbol{d}|)$ in Eq. (6) is applied to scale this feature within the range $[-1,1]$. That is, first, $d_i$ is calculated when neglecting the

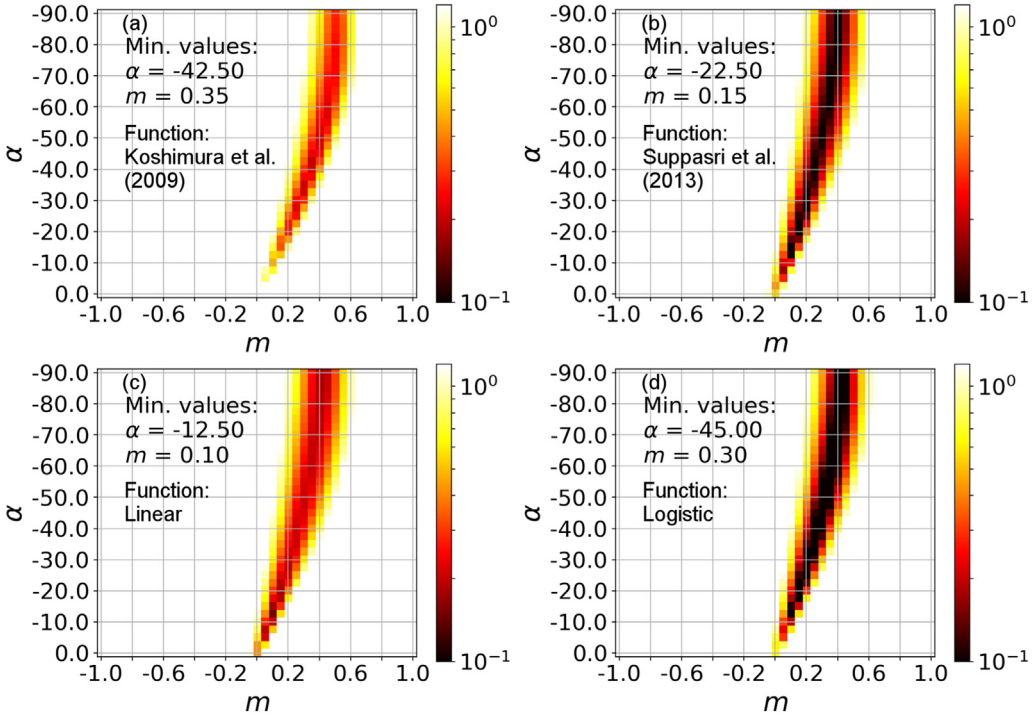


**Fig. 5.** Cost function calculated using different fragility functions. (a) Koshimura et al. [13]; (b) Suppasri et al. [23]; (c) Linear; (d) Logistic.

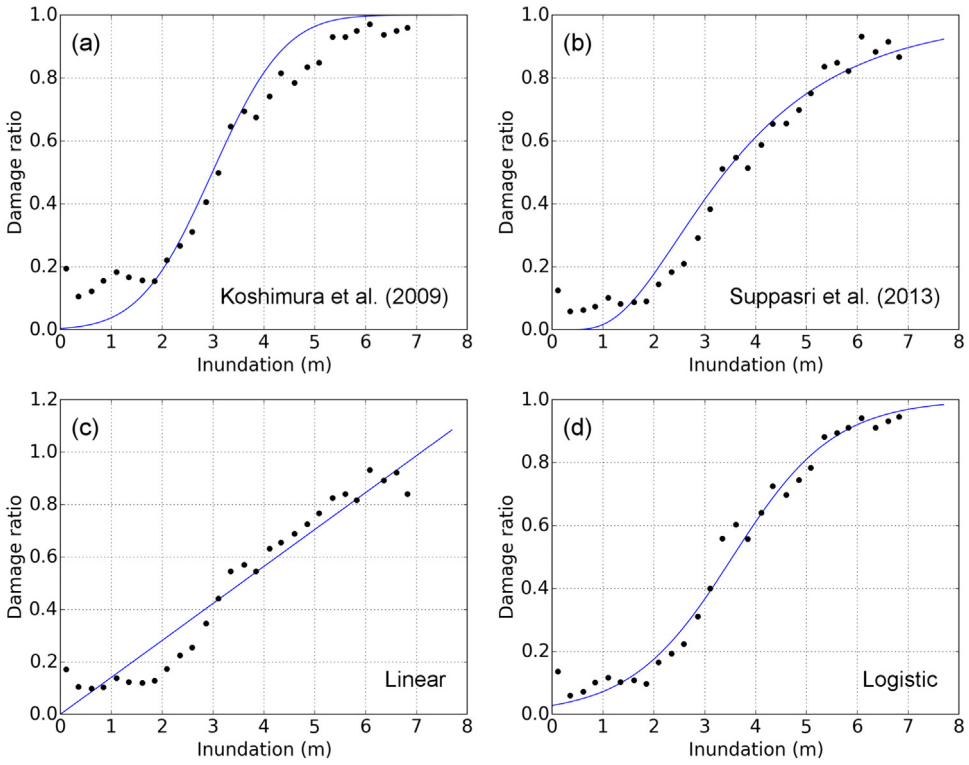


**Fig. 6.** Ratio of collapsed buildings vs the inundation depth obtained from the results (dark marks) and fragility function used for the calibration of the threshold function (solid line).

referred term. Then, the values are scaled by dividing the maximum value of $|d_i|$. Fig. 4a shows a scatter plot of the complete bi-dimensional feature database. Fig. 4b–h show the same data separated by building damage state according to MLIT. The color mark depicts the point density, and the lightest color shows the highest density. The clustering of marks tends to move to a large value of $r$ and a value of $d$ of zero when the damage state decreases. However, there is clear overlap between the collapsed buildings (DS6) and the other buildings (DS0–DS5).

In this study, a linear threshold function was used and is defined by the slope angle $\alpha$ and its distance to the origin of coordinates $m$. For instance, Fig. 4(a) shows a set of threshold candidates with $\alpha = -45$ and $m$ at intervals of 0.2. Therefore, in this case study the cost function

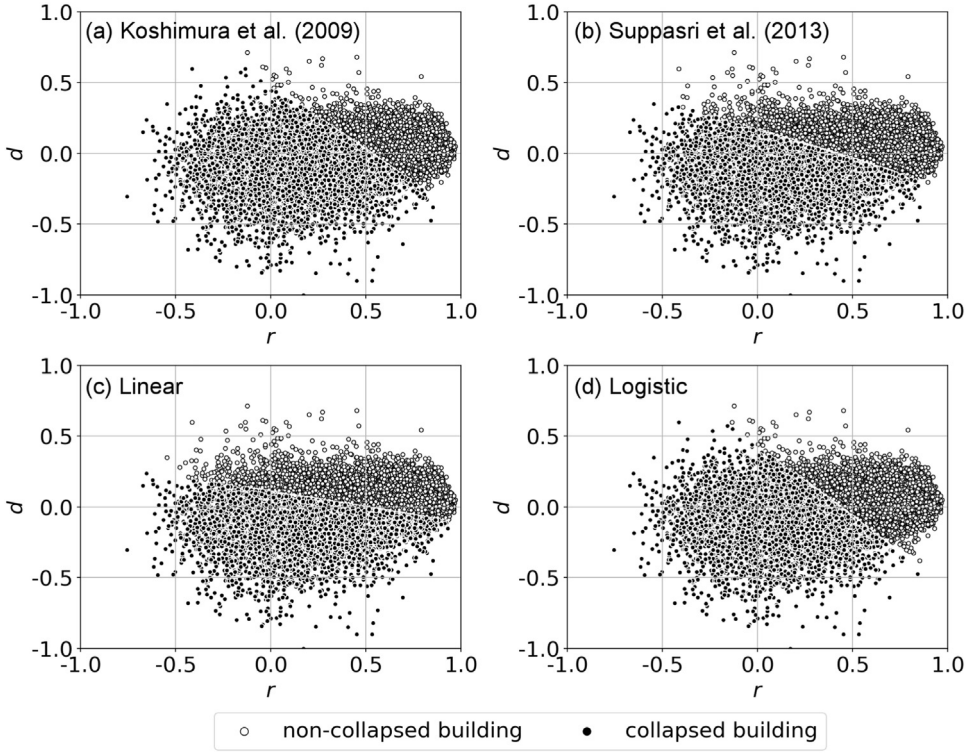


**Fig. 7.** Scatter plot of collapsed (dark dots) and non-collapsed buildings (white dots) according to the final threshold function.

depends of two variables. The cost function was calculated from a grid search approach. The colormap shown in Fig. 5 depicts the cost function for a range values of $\alpha$ and $m$. The parameters that yielded the minimum cost function using the four fragility functions (Eqs. (2)–(5)) are also shown. The result using Koshimura et al. [13]'s fragility function ($\alpha = -42.5$, $m = 0.35$) and the logistic function ($\alpha = -45.0$, $m = 0.30$) are very similar. Fig. 6 shows the change ratio for different levels of inundation depth resulting from the optimal threshold function. The fragility function used during the methodology is shown as a solid line as well. As can be observed, the methodology found the parameters $\alpha$ and $m$ that best fit the fragility functions. Fig. 7 shows the scatter plot of the binary classification, collapsed and non-collapsed buildings, using the threshold function as the decision boundary. At first glance, it seems that the methodology is not working properly because of the differences between the threshold functions. It seems that the linear thresholds resulting from Suppasri et al. [23] and the linear function (Figs. 7b and 7c) cover a larger region of non-collapsed buildings compared with the results using Koshimura et al. [13] and the logistic function (Figs. 7a and 7d). However, the common regions for collapsed and non-collapsed building from the four results are the regions in which the majority of the data is concentrated. This pattern is confirmed in Fig. 4b–h, in which the final linear thresholds are shown together with features separates by damage states. Buildings with damage states 0–4 are well classified as non-collapsed by the four fragility curves. Similarly, the main portion of buildings with a damage state of 6 are classified as collapsed buildings. The main discrepancies are observed in buildings with DS5, the majority of which are classified as non-collapsed. Fig. 8 shows a closer look at the collapsed building map from the surveyed data and that estimated by the proposed method. A good agreement between these data is observed.

### 3.4. Accuracy assessment

The verification of our estimations was performed by comparing them with the surveyed building damage inventory provided by the MLIT. Tables 2–5 summarizes the comparison of our estimations and the ground truth data. Here typical scores, such as overall accuracy, user accuracy and producer accuracy, are calculated for the evaluation. Overall accuracy (OA) is the ratio between the number of samples correctly classified and the total number of samples. For a given class, let say $I$, the user accuracy (UA) is the ratio of the number of samples correctly classified as $I$ to the number of samples classified as $I$. The producer accuracy (PA) is the ratio of samples correctly classified as $I$ to the number of samples that truly belongs to class $I$. As mentioned before, the ground truth data provides a great amount of detail with 7 damage states, DS0–DS6; however, our method performs a binary classification: collapsed and non-collapsed buildings. Therefore, for accuracy evaluation, DS0–DS5 were merged to one group: non-collapsed buildings. When the method was applied using Koshimura et al. [13]'s fragility function, the OA was 81.4%, with a PA of 92.7% and UA of 61.2% for collapsed buildings. When the method was applied using Suppasri et al. [23]'s fragility function, the OA was 84.9% with a PA of 81.8% and UA of 69.8% for collapsed buildings. When the method was applied using a linear fragility function, the OA was 80.8% with a PA of 80% and UA of 62.4% for collapsed buildings. When the method was applied using a logistic fragility function, the OA was 85.5% with a PA of 87.7% and UA of 69.2% for collapsed buildings. The Cohen's kappa coefficient was 0.60, 0.64, 0.56, and 0.67 for the results using the approaches in Koshimura et al. [13], and Suppasri et al. [23] and the linear and logistic functions, respectively (Table 6).

A notable difference between PA and UA is observed. Tables 2–5 also show the errors of non-collapsed buildings separated by different damage states (DS0–DS5). Buildings classified as DS5 show the highest error, which is the main cause of the low UA.

## 4. Discussion

Regarding the calculation of the features, using a bigger region than the footprint, two issues were solved: First, the inclusion of the layover and shadowing information. As mentioned before, because of the side-looking nature of SAR, a building produces layover effects outside the building and in the direction of the SAR sensor; furthermore, shadowing

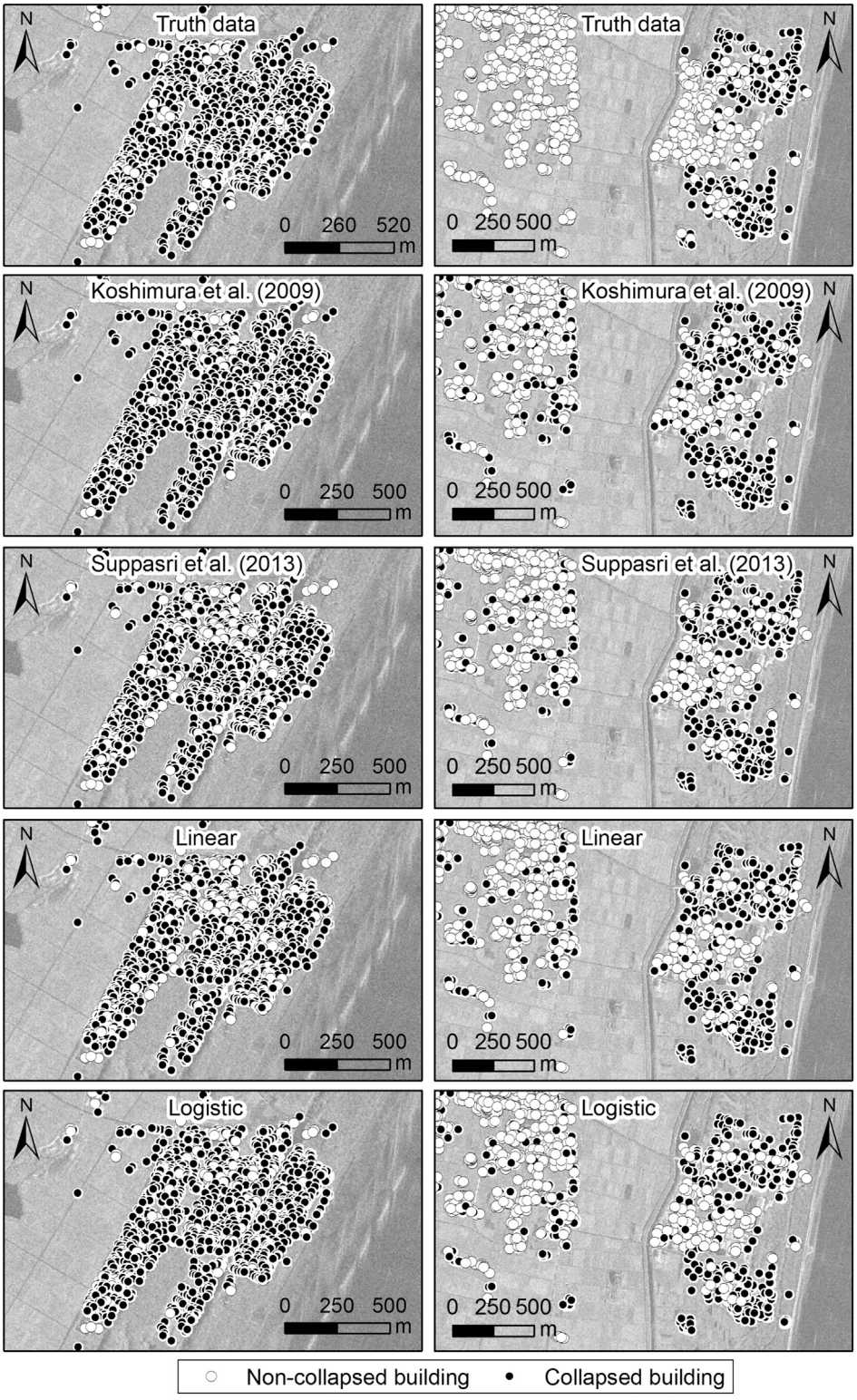


**Fig. 8.** Closer look at collapsed buildings map. Left column corresponds to region (i), and right column corresponds to region (ii); both are shown in Fig. 3b.

is produced in the opposite side. Liu et al. [1] considered the effect of layover by shifting certain values in the footprint database towards the direction of the sensor. In this paper, however, it was decided to consider both the layover and the shadowing effects by increasing the building footprint. The second issue was the discrepancy between the location of the buildings in the vector database and that in the SAR images. It was found that these locations were not a perfect match. Thus, by increasing the footprint, the backscattering of the complete building would be included. The main drawback in increasing the building footprint is that it might include fractions of neighboring buildings. However, the calculated features $d$ and $r$ represent an aggregate value of the rectangular box used for their calculations, and thus, it should not affect the results significantly. This assumption is verified in the scatter plot of Fig. 4, in which the collapsed and non-collapsed buildings tend to be grouped in different regions.

Moreover, a significant misclassification of buildings as DS5 was

**Table 2**
Accuracy of damage detection using Koshimura et al.'s reference function.

| | DS0 | DS1 | DS2 | DS3 | DS4 | DS5 | DS0–DS5 | DS6 | Total | UA |
|---|---|---|---|---|---|---|---|---|---|---|
| NC | 1646 | 2184 | 5640 | 4738 | 1147 | 1905 | **17,260** | **643** | **17,903** | **96.4** |
| C | 211 | 394 | 1009 | 1282 | 548 | 1727 | **5171** | **8161** | **13,332** | **61.2** |
| Total | 1857 | 2578 | 6649 | 6020 | 1695 | 3632 | **22,431** | **8804** | **31,235** | |
| PA | 88.6 | 84.7 | 84.8 | 78.7 | 67.7 | 52.5 | **76.9** | **92.7** | | **81.4** |

**Table 3**
Accuracy of damage detection using Suppasri et al.'s reference function.

| | DS0 | DS1 | DS2 | DS3 | DS4 | DS5 | DS0–DS5 | DS6 | Total | UA |
|---|---|---|---|---|---|---|---|---|---|---|
| NC | 1739 | 2362 | 6131 | 5252 | 1353 | 2471 | **19,308** | **1602** | **20,910** | **92.3** |
| C | 118 | 216 | 518 | 768 | 342 | 1161 | **3123** | **7202** | **10,325** | **69.8** |
| Total | 1857 | 2578 | 6649 | 6020 | 1695 | 3632 | **22,431** | **8804** | **31,235** | |
| PA | 93.6 | 91.6 | 92.2 | 87.2 | 79.8 | 68.0 | **86.1** | **81.8** | | **84.9** |

**Table 4**
Accuracy of damage detection using a linear reference function.

| | DS0 | DS1 | DS2 | DS3 | DS4 | DS5 | DS0–DS5 | DS6 | Total | UA |
|---|---|---|---|---|---|---|---|---|---|---|
| NC | 1630 | 2248 | 5922 | 4929 | 1251 | 2185 | **18,165** | **1722** | **19,887** | **91.3** |
| C | 227 | 330 | 727 | 1091 | 444 | 1447 | **4266** | **7082** | **11,348** | **62.4** |
| Total | 1857 | 2578 | 6649 | 6020 | 1695 | 3632 | **22,431** | **8804** | **31,235** | |
| PA | 87.8 | 87.2 | 89.1 | 81.9 | 73.8 | 60.2 | **81.0** | **80.4** | | **80.8** |

**Table 5**
Accuracy of damage detection using a logistic reference function.

| | DS0 | DS1 | DS2 | DS3 | DS4 | DS5 | DS0–DS5 | DS6 | Total | UA |
|---|---|---|---|---|---|---|---|---|---|---|
| NC | 1747 | 2337 | 6008 | 5193 | 1339 | 2367 | **18,991** | **1079** | **20,070** | **94.6** |
| C | 110 | 241 | 641 | 827 | 356 | 1265 | **3440** | **7725** | **11,165** | **69.2** |
| Total | 1857 | 2578 | 6649 | 6020 | 1695 | 3632 | **22,431** | **8804** | **31,235** | |
| PA | 94.1 | 90.7 | 90.4 | 86.3 | 79.0 | 65.2 | **84.7** | **87.7** | | **85.5** |

**Table 6**
Cohen's kappa coefficient ($\kappa$).

| | Koshimura et al. | Suppasri et al. | Linear | Logistic |
|---|---|---|---|---|
| $\kappa$ | 0.60 | 0.64 | 0.56 | 0.67 |

also observed, which was the main cause of the low UA. Perhaps the main reason for this misclassification is the definition of DS5. According to Suppasri et al. [23], DS5 is classified as *collapsed*. However, the description was *"Destructive to walls (more than half of wall density) and several columns (bend or destroyed)"* and the condition was *"Loss of functionality (system collapse). Non-reparable or great cost for retrofitting"*. This definition is considered from the perspective of a structural engineer. Structurally speaking, a collapsed buildings refers to a building for which the structural system has been severely compromised; however, it can still be standing up. According to FEMA 356 [26], a wooden building is considered collapsed when the story drift is greater than 3%. Thus, for a wooden house of 2 stories at 4 m each, the minimum drift to be considered collapsed is $2 \times 3\% \times 4\,\text{m} = 24\,\text{cm}$. However, recall that the resolution of the SAR imagery used in this study was 1.25 m. This fact reflects the limitations of the sensor rather than limitations of the methodology. Therefore, the majority of DS5 buildings will not be detected by SAR images; however, buildings with significant distortions might produce enough changes in the backscattering to be classified as collapsed. On the other hand, DS6 buildings are classified as *"Washed away"*, the definition of which is *"Washed away, only foundation remains, totally overturned"* and the condition is *"Non-repairable, requires total reconstruction"*. Collapsed buildings with these characteristics are certainly detected by SAR imagery. Thus, we believe that our results are consistent with the surveyed dataset.

With respect to the methodology. In this study, the parameters of the threshold function ($\alpha$ and $m$) were found from a grid search (Fig. 5). Although it was not an efficient procedure, it did not require much computational effort considering the two-dimensional case. A grid search provides information regarding the shape of the cost function. In the case study, the cost function showed a convex shape independent of the fragility function used. The proposed methodology can be modified for databases with more than 2 features. For instance, in cases where SAR imagery from different sensors is available, such as the X-band from TerraSAR, C-band from Sentinel-1, L-band from ALOS-2, the dimensionality of the dataset will increase significantly. In this case, a better algorithm for finding the minimum cost function should be used.

The methodology was designed for binary classifications. However, intermediate damage states can be estimated by the subsequent application of the proposed method. For instance, for three levels of damage, say severe, moderate and non-damage, the method is applied first to identify the buildings with severe damage; then the method is applied again in the buildings without severe damage to identify buildings with moderate damage and buildings without damage. Fragility curves for severe and moderate damage is required for this purpose. In practice, the applicability of the method to identify intermediate level of damage is limited by the resolution of the satellite images. As mentioned before, the TerraSAR-X images used in the case study have a resolution of 1.25 m; and thus, it is not possible to detect cracks or distortions in the buildings.

One issue regarding the case study is the assumption that the tsunami event was the dominant event compared with the ground motion

due to the earthquake. Thus, it was inferred that the collapsed buildings were produced by the tsunami. Recall that the source-rupture process caused large ground acceleration in a wide area of northern Japan [27]; however, the collapsed buildings were concentrated in the tsunami inundated area.

In the case study, we used two fragility functions based on empirical information and numerical simulations of real tsunami events: Koshimura et al. [13] and Suppasri et al. [23]. Both fragility functions achieved results that were consistent with the surveyed data, showing an overall accuracy of 81.4% and 84.9%. However, it is strongly recommended to use fragility functions conceived for the target area. Furthermore, two additional functions were tested for use as fragility functions: a linear and logistic function. It is worth noting that a linear relation between the damage ratio and the engineering demand has never been observed. However, it is desirable to examine the results when an inappropriate fragility function is used. For the linear relation, a 100% change ratio was assumed for an inundation depth of 7.1 m (Fig. 6c), which was the maximum inundation depth for a significant number of buildings. Although the use of a linear function produced the lowest accuracy, the agreement with the ground truth data was acceptable. On the other hand, the use of a logistic function produced the highest accuracy. Following the same approach, a logistic function with a 50% change ratio for an inundation depth of 3.55 m (Fig. 6) was used in order to achieve a large percentage of change ratio at an inundation depth of 7.1 m.

Currently, the framework is implemented in Python Language Program. In a HP Z240 SFF Workstation (3.70 GHz), the extraction of the features took 46.2 s and the calibration of the threshold function took 182.3 s. We believe this runtime s short enough for emergency response. However, the runtime can be reduced after moving the code to a compiled language, such as Fortran or C++.

Finally, we would like to emphasize that the proposed method must be implemented within a quick response framework after a natural disaster. That is to say, the appropriate fragility curve and the geospatial building database should be available in advance and ready for use at all times. In the aftermath of a natural disaster, the framework must focus on retrieving the satellite imagery and the distribution of EDP for the subsequent application of the proposed method.

## 5. Conclusions

Based on satellite imagery, the spatial distribution of the demand and fragility functions, and building inventory, this paper presents a novel collapsed building extraction method. This method overcomes some of the disadvantages of the previous approaches to extract building damage using satellite images. For instance, this approach does not require manual intervention to define a boundary decision function. Furthermore, unlike the standard machine learning algorithms, the method does not require training data, which are extremely difficult to retrieve right after a natural disaster event. It is also adaptable to n-dimensional datasets.

The method has been applied to the 2011 Great East Japan Tsunami in Miyagi Prefecture. Two high-resolution TerraSAR-X intensity images taken before and after the event were used. From the SAR images, together with a geocoded building data inventory, two features were calculated, the average difference in backscattering $d$ and the correlation coefficient $r$, for each building. The spatial distribution of inundation depth was used as the demand parameter. Collapsed buildings were detected and compared with the building damage inventory provided by the Ministry of Land, Infrastructure and Transportation (MLIT). The method achieved an overall accuracy ranging from 80.8% (using a linear fragility function) to 85.5% (using a logistic fragility function). It is necessary however, to test the performance of the proposed methodology in other kind of disaster events and other type of sensors. Currently, these issues represent our future work. Furthermore, the effects of the uncertainties on the numerical simulation of the hazard in the results will be addressed in a future paper.

## References

[1] W. Liu, F. Yamazaki, H. Gokon, S. Koshimura, Extraction of tsunami-flooded areas and damaged buildings in the 2011 Tohoku-Oki earthquake from terrasar-x intensity images, Earthq. Spectra 29 (S1) (2013) S183–S200, http://dx.doi.org/10.1193/1.4000120.

[2] M. Matsuoka, N. Nojima, Building damage estimation by integration of seismic intensity information and satellite l-band sar imagery, Remote Sens. 2 (9) (2010) 2111–2126, http://dx.doi.org/10.3390/rs2092111 ⟨http://www.mdpi.com/2072-4292/2/9/2111⟩.

[3] W. Liu, F. Yamazaki, Extraction of collapsed buildings in the 2016 Kumamoto earthquake using multi-temporal palsar-2 data, J. Disaster Res. 12 (2) (2017) 241–250, http://dx.doi.org/10.20965/jdr.2017.p0241.

[4] S. Karimzadeh, M. Mastuoka, Building damage assessment using multisensor dual-polarized synthetic aperture radar data for the 2016 m 6.2 Amatrice earthquake, Italy, Remote Sens. 9 (4) (2017), http://dx.doi.org/10.3390/rs9040330 ⟨http://www.mdpi.com/2072-4292/9/4/330⟩.

[5] Union of Concerned Scientist, UCS Satellite Database, 2017. Available at ⟨http://www.ucsusa.org/nuclear-weapons/space-weapons/satellite-database?_ga=2.222644636.626569541.1506392035-1335092672.1506392035#.Wcm38LIjFaQ⟩, (Online; Accessed 26 September 2017).

[6] Digital Globe, Open Data Program, 2017. Available at ⟨https://www.digitalglobe.com/opendata⟩, (Online; Accessed 26 September 2017).

[7] H. Gokon, S. Koshimura, M. Matsuoka, Object-based method for estimating tsunami-induced damage using terrasar-x data, J. Disaster Res. 11 (2) (2016) 225–235, http://dx.doi.org/10.20965/jdr.2016.p0225.

[8] H. Gokon, S. Koshimura, K. Meguro, Verification of a method for estimating building damage in extensive tsunami affected areas using l-band sar data, J. Disaster Res. 12 (2) (2017) 251–258, http://dx.doi.org/10.20965/jdr.2017.p0251.

[9] M. Wieland, W. Liu, F. Yamazaki, Learning change from synthetic aperture radar images: performance evaluation of a support vector machine to detect earthquake and tsunami-induced changes, Remote Sens. 8 (10) (2016), http://dx.doi.org/10.3390/rs8100792.

[10] S. Ozawa, T. Nishimura, H. Suito, T. Kobayashi, M. Tobita, T. Imakiire, Coseismic and postseismic slip of the 2011 magnitude-9 Tohoku-Oki earthquake, Nature 471 (S1) (2011) S373–S376, http://dx.doi.org/10.1038/nature10227.

[11] M. Hashimoto, Crustal deformation associated with the 2011 Tohoku-Oki earthquake: an overview, Earthq. Spectra 29 (S1) (2013) S81–S98, http://dx.doi.org/10.1193/1.4000117.

[12] L. Moya, F. Yamazaki, W. Liu, Comparison of coseismic displacement obtained from geonet and seismic networks, J. Earthq. Tsunami 10 (2) (2016) 1640002, http://dx.doi.org/10.1142/S1793431116400029.

[13] S. Koshimura, T. Oie, H. Yanagisawa, F. Imamura, Developing fragility functions for tsunami damage estimation using numerical model and post-tsunami data from Banda Aceh, Indonesia, Coast. Eng. J. 51 (3) (2009) 243–273, http://dx.doi.org/10.1142/S0578563409002004.

[14] D. Melgar, Y. Bock, Near-field tsunami models with rapid earthquake source inversions from land- and ocean-based observations: the potential for forecast and warning, J. Geophys. Res.: Solid Earth 118 (11) (2013) 5939–5955, http://dx.doi.org/10.1002/2013JB010506.

[15] D. Melgar, Y. Bock, Kinematic earthquake source inversion and tsunami runup prediction with regional geophysical data, J. Geophys. Res.: Solid Earth 120 (5) (2015) 3324–3349, http://dx.doi.org/10.1002/2014JB011832.

[16] A. Martinelli, G. Cifani, G. Cialone, L. Corazza, A. Petracca, G. Petrucci, Building vulnerability assessment and damage scenarios in Celano (Italy) using a quick survey data-based methodology, Soil Dyn. Earthq. Eng. 28 (10) (2008) 875–889 (Special Issue: Urban Earthquake Hazard and Damage Assessment), ⟨https://doi.org/10.1016/j.soildyn.2008.03.002⟩.

[17] A.C. Zülfikar, N.Ö.Z. Fercan, S. Tunç, M. Erdik, Real-time earthquake shake, damage, and loss mapping for istanbul metropolitan area, Earth Planets Space 69 (1) (2017) 9, http://dx.doi.org/10.1186/s40623-016-0579-x.

[18] S. Karimzadeh, B. Feizizadeh, M. Matsuoka, From a gis-based hybrid site condition map to an earthquake damage assessment in Iran: methods and trends, Int. J. Disaster Risk Reduct. 22 (Suppl. C) (2017) S23–S36 ⟨https://doi.org/10.1016/j.ijdrr.2017.02.016⟩.

[19] N.I. Frolova, V.I. Larionov, J. Bonnin, S.P. Sushchev, A.N. Ugarov, M.A. Kozlov, Seismic risk assessment and mapping at different levels, Nat. Hazards 88 (1) (2017) 43–62, http://dx.doi.org/10.1007/s11069-016-2654-9.

[20] Y. Maruyama, F. Yamazaki, K. Mizuno, Y. Tsuchiya, H. Yogai, Fragility curves for expressway embankments based on damage datasets after recent earthquakes in Japan, Soil Dyn. Earthq. Eng. 30 (11) (2010) 1158–1167, http://dx.doi.org/10.1016/j.soildyn.2010.04.024.

[21] F. Yamazaki, O. Murao, Vulnerability functions for Japanese buildings based on damage data from the 1995 Kobe earthquake, in: A.S. Elnashai, S. Antoniou (Eds.), Vol. 2 of Implications of Recent Earthquakes on Seismic Risk, Imperial College Press, London, 2000.

[22] K. Porter, R. Kennedy, R. Bachman, Creating fragility functions for performance-based earthquake engineering, Earthq. Spectra 23 (2) (2007) 471–489, http://dx.doi.org/10.1193/1.2720892.

[23] A. Suppasri, E. Mas, I. Charvet, R. Gunasekera, K. Imai, Y. Fukutani, Y. Abe, F. Imamura, Building damage characteristics based on surveyed data and fragility curves of the 2011 Great East Japan tsunami, Nat. Hazards 66 (2) (2013) 319–341, http://dx.doi.org/10.1007/s11069-012-0487-8.

[24] E. Mas, S. Koshimura, A. Suppasri, M. Matsuoka, M. Matsuyama, T. Yoshii, C. Jimenez, F. Yamazaki, F. Imamura, Developing tsunami fragility curves using remote sensing and survey data of the 2010 Chilean tsunami in Dichato, Nat. Hazards Earth Syst. Sci. 12 (8) (2012) 2689–2697, http://dx.doi.org/10.5194/nhess-12-2689-2012.

[25] D. Brunner, G. Lemoine, L. Bruzzone, Earthquake damage assessment of buildings using vhr optical and sar imagery, IEEE Trans. Geosci. Remote Sens. 48 (5) (2010) 2403–2420, http://dx.doi.org/10.1109/TGRS.2009.2038274.

[26] FEMA 356, Prestandard and Commentary for the Seismic Rehabilitation of Buildings, Federal Emergency Management Agency, Washington, D.C., 2000.

[27] T. Furumura, S. Takemura, S. Noguchi, T. Takemoto, T. Maeda, K. Iwai, S. Padhy, Strong ground motions from the 2011 off-the Pacific-Coast-of-Tohoku, Japan (mw = 9.0) earthquake obtained from a dense nationwide seismic network, Landslides 8 (3) (2011) 333, http://dx.doi.org/10.1007/s10346-011-0279-3.